

Uncovering the Different Components of Contact Resistance to Atomically Thin Semiconductors

Emanuel Ber, Ryan W. Grady, Eric Pop, and Eilam Yalon*

Achieving good electrical contacts is one of the major challenges in realizing devices based on atomically thin 2D semiconductors. Several studies have examined this hurdle, but a universal understanding of the contact resistance (R_c) and an underlying approach to its reduction are currently lacking. Here, the classical R_c transmission line model description of contacts to 2D materials is experimentally examined, and a modification based on an additional lateral resistance component, namely, the junction resistance (R_{jun}) is offered. A combination of transfer length method and contact-end measurements to characterize contacts to monolayer MoS₂ and separate the different R_c components is used. Technology computer-aided design simulations are also used to study R_c in Fermi-level pinned and unpinned contacts. This study finds that R_{jun} is the dominating component of R_c in atomically thin semiconductor devices, and is also responsible for most of the back-gate bias and temperature dependence. The experimental results help understand the underlying physics of state-of-the-art contact engineering in the context of minimizing R_{jun} .

lateral dimensions of field effect transistors (FETs) decrease, other dimensions must follow suit to retain electrostatic gate control.^[3,4] However, reducing the thickness of transistor channels below ≈ 4 nm raises difficulties for conventional bulk semiconductors.^[5] 2D semiconductors are therefore considered prime candidates for ultrathin channels thanks to their few-atom thickness, alongside other advantages (e.g., heterogenous integration, substrate independence, and more).^[6–8] Among the main difficulties in realizing transistors, solar cells, or other electronic devices based on 2D materials is the high contact resistance (R_c), hindering transistor output current and affecting V_{oc} and J_{sc} in solar cells.^[8,9] Recent works have proposed reducing R_c using approaches such as varying the contact material and doping.^[10–17] However, how each approach affects the measured R_c remains poorly

1. Introduction

For five decades silicon-based complementary metal-oxide-semiconductor (CMOS) technologies have relied on reducing the size of transistors to increase their density on a chip, enabling a steady increase in computation capability.^[1,2] As the

understood. Therefore, a universal method to understand and identify the contact resistance bottleneck is key for future contact engineering and matching the resistance reduction method to the underlying cause.

Classically, an electrical contact between a metal and semiconductor is described by its R_c , which depends on the specific contact resistivity (ρ_c) and the sheet resistance under the contact (R_{sk}), as seen in **Figure 1a**.^[18] Note that R_{sk} is generally different from the sheet resistance in the channel (R_{sh}), stemming from the various contact formation processes (e.g., silicidation, doping, contact deposition) that can affect the region under the contact.^[19] These processes are expected to have a more severe impact on atomically thin 2D FETs where significant structural damage to monolayers due to contact metal evaporation has been reported.^[20–22] The simple contact resistance model cannot capture two important phenomena that occur in contacts to 2D semiconductors: a) band bending due to the presence of a barrier (e.g., Schottky) must extend laterally into the channel,^[23–25] and b) doping the access regions of 2D FETs is known to reduce their measured R_c .^[11,12,26,27] So far, studies have explained the dependency of R_c in these phenomena by suggesting a two-path injection mechanism,^[24,28,29] but there has yet to be an implementation of these effects into the contact resistance model.

In this study we present a novel experimental analysis of monolayer MoS₂ transistors that uncovers a discrepancy in the contact characterization by the classical contact resistance model, which does not exist in bulk materials. We offer

E. Ber, E. Yalon
 Viterbi Faculty of Electrical and Computer Engineering
 Technion-Israel Institute of Technology
 Haifa 32000, Israel
 E-mail: eilamy@technion.ac.il

R. W. Grady, E. Pop
 Department of Electrical Engineering
 Stanford University
 Stanford, CA 94305, USA

E. Pop
 Department of Materials Science and Engineering
 Stanford University
 Stanford, CA 94305, USA

 The ORCID identification number(s) for the author(s) of this article can be found under <https://doi.org/10.1002/aelm.202201342>.

© 2023 The Authors. Advanced Electronic Materials published by Wiley-VCH GmbH. This is an open access article under the terms of the Creative Commons Attribution License, which permits use, distribution and reproduction in any medium, provided the original work is properly cited.

DOI: 10.1002/aelm.202201342

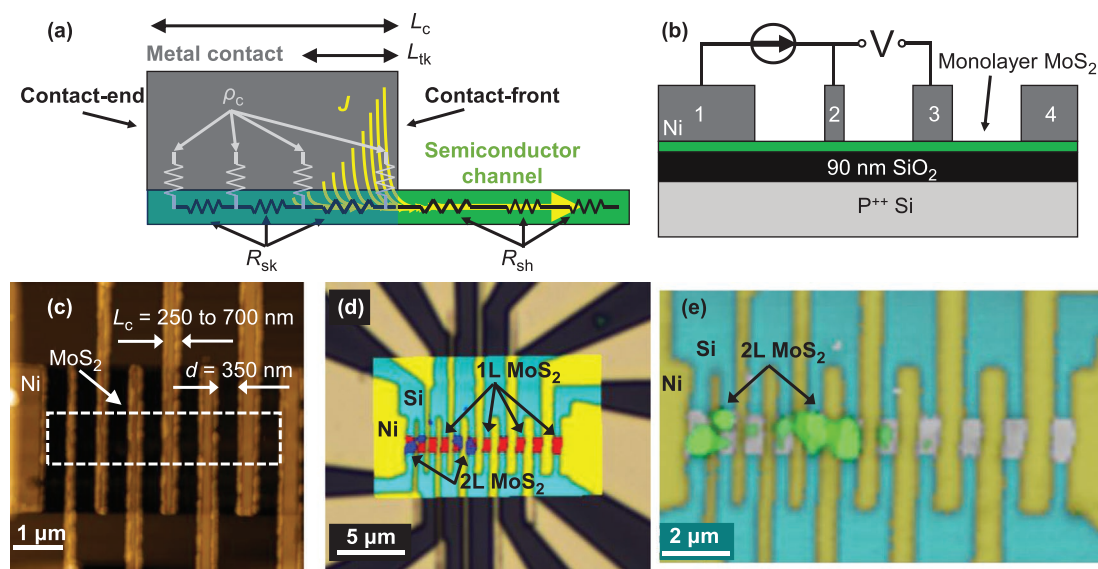


Figure 1. Transmission line model parameters and contact-end measurements structure. a) Resistance network according to the classic contact resistance model (note that R_{jun} is not present in the classic model) along the current path from a semiconductor channel to the metal contact. R_{sh} is the semiconductor channel sheet resistance, R_{sk} is the semiconductor sheet resistance under the contacts, and ρ_c is the specific contact resistivity. The shaded area under the contact represents the difference in properties induced by the presence of the metal. The effective transfer length is noted by L_{tk} , and the physical contact length is L_c . Yellow arrows represent current flow paths. b) Schematic cross-section of the CER test structure, and the measurement probing setup. c) AFM image of the fabricated structures with equally distanced contacts ($d = 350$ nm) and varying contact lengths ($L_c = 250\text{--}700$ nm). d) Raman and e) second harmonic generation mapping of the same CER structure overlaid on top of an optical microscopy image. Most of the channel is 1L with some 2L islands. The 2L channels are excluded from our analysis to prevent variations in the extracted data.

a correction to the model, modifying it to accurately detail Fermi-level pinned contacts to atomically thin 2D semiconductors. Our thorough examination of the contacts was carried out with transfer length method (TLM), contact-end resistance (CER), and four-point probe (4PP) measurements.^[18] The combination of these three techniques allowed, for the first time, the separation and characterization of the vertical and lateral current injection resistances.

Our results suggest that in addition to ρ_c and R_{sk} , the intrinsic resistance components of the metal-semiconductor interface, a lateral resistance component must be introduced to explain the total contact resistance to 2D materials. Technology computer-aided design (TCAD) simulations were used to explore the barrier extension into the channel and the behavior of R_c for pinned and unpinned contacts. We adopt the junction resistance (R_{jun}) concept proposed by Venica et al.^[30] and expand it to include the lateral current injection resistance. The junction resistance accounts for the injection over or through the Schottky barrier which extends into the channel, as well as the properties of the semiconductor under the contacts and in the access region. Therefore, R_{jun} encompasses the contribution of the two factors, directly connecting access region doping and contact metal variation to R_c . The implementation of R_{jun} into the corrected contact resistance model can universally explain recent state-of-the-art data reported in the literature, unifying the physical origin of the contact resistance reduction of the various contact engineering methods.

2. Results and Discussion

2.1. TLM and Contact-End Resistance Measurements

An important parameter of contacts with “lateral” current flow is the average length which carriers travel inside the semiconductor before they are vertically injected into the metal,^[18,31] named the effective transfer length (L_{tk}) and illustrated in Figure 1a. It originates from the potential distribution under the contact which is given by^[18,32]

$$V(x) = \frac{I\sqrt{R_{\text{sk}}\rho_c}}{W} \frac{\cosh[(L_c - x)/L_{\text{tk}}]}{\sinh(L_c/L_{\text{tk}})} \quad (1)$$

where I is the current flowing into the contact, W is the contact width, and L_c is the contact length. We see that most of the carrier injection takes place near the contact-front (i.e., the channel side of the contact), and decays across the length of the contact, with a characteristic distance L_{tk} , which is given by

$$L_{\text{tk}} = \sqrt{\rho_c/R_{\text{sk}}} \quad (2)$$

and is thus a product of the intrinsic parameters of the contact, ρ_c and R_{sk} . The voltage drop at the contact-front divided by the applied current results in the contact-front resistance (R_{cf}), given by

$$R_{\text{cf}} = \frac{V_{x=0}}{I} = \frac{\sqrt{R_{\text{sk}}\rho_c}}{W} \coth(L_c/L_{\text{tk}}) \approx \frac{\sqrt{R_{\text{sk}}\rho_c}}{W} = \frac{\rho_c}{L_{\text{tk}}W} \quad (3)$$

where the right-hand side approximation is valid for test structures where the physical contact length, L_c , is large enough compared to L_{tk} ($L_c \gg L_{tk}$). The voltage drop near the contact-end (i.e., the side of the contact opposite to the channel) divided by the applied current results in the contact-end resistance (R_{ce}), given by

$$R_{ce} = \frac{V_{x=L_c}}{I} = \frac{\sqrt{R_{sk}\rho_c}}{W} \frac{1}{\sinh(L_c/L_{tk})} \approx \frac{2\sqrt{R_{sk}\rho_c}}{W} e^{(-L_c/L_{tk})} = \frac{2\rho_c}{L_{tk}W} e^{(-L_c/L_{tk})} \quad (4)$$

and can therefore be used to extract R_{sk} and ρ_c , as previously mentioned. The right-hand side approximation is again valid for $L_c > L_{tk}$, however only in structures where L_c is on the same order of L_{tk} ($L_c \sim L_{tk}$) there is a significant and measurable voltage drop at the contact-end.

The most common method of contact characterization is the TLM measurement, which is traditionally used to separate R_{sh} from R_c .^[18,19] However, this measurement does not provide information about the distribution between ρ_c and R_{sk} without the assumption that $R_{sk} = R_{sh}$,^[19] which should not be the case for contacts to 2D channels, as discussed above. To circumvent this assumption, we utilize CER measurements which in conjunction with data from TLM measurements allow us to independently characterize R_c , R_{sh} , R_{sk} , and ρ_c . A schematic representation of a CER device structure is given in Figure 1b. We perform CER measurements by applying current I_{12} between terminals 1 and 2 and probing the voltage drop V_{23} between terminals 2 and 3, see Section S1 (Supporting Information) for more information. The measured contact-end resistance is then

$R_{ce} = V_{23}/I_{12}$. For device fabrication we grew monolayer (1L) MoS₂ by chemical vapor deposition^[33] (CVD) on SiO₂ (90 nm) on Si (p⁺⁺), and evaporated Ni as contacts. The highly doped Si substrate serves as a global back-gate, see the Experimental Section for more information.

Figure 1c shows an atomic force microscopy (AFM) image of our CER measurement structure where the contacts are equally spaced ($d = 350$ nm) and vary in length ($L_c = 250$ – 700 nm). Section S2 (Supporting Information) presents length measurements performed on the AFM scan images that determine d and L_c . Figure 1d,e shows Raman and second harmonic generation (SHG) mapping measurements that exhibit good agreement between them, confirming that most channels consist of 1L MoS₂, with some scattered bilayer (2L) islands. SHG mapping is highly sensitive to the number and relative orientation of 2D-material-layers, thus helping with the characterization.^[34–36] We expect the 2L areas to result in some variation in our extracted data, therefore these channels are excluded from our analysis. More details on the Raman and SHG spectroscopy are available in Section S3 (Supporting Information).

Figure 2a shows I_D versus V_{GS} measurements of a 1 μm long channel from a TLM array, performed in vacuum ambient condition ($<10^{-4}$ mbar) at room temperature and cryogenic conditions, presented in linear and log scale. These characteristics show typical back-gate control with $I_{on}/I_{off} \approx 10^7$, and 43 $\mu\text{A } \mu\text{m}^{-1}$ current at $V_{GS} = 40$ V and $V_{DS} = 1$ V, at room temperature. We measured no notable hysteresis, and the gate leakage current was negligible ($I_G < 5$ pA). To account for the variance in electrical properties between different channels in the TLM arrays,

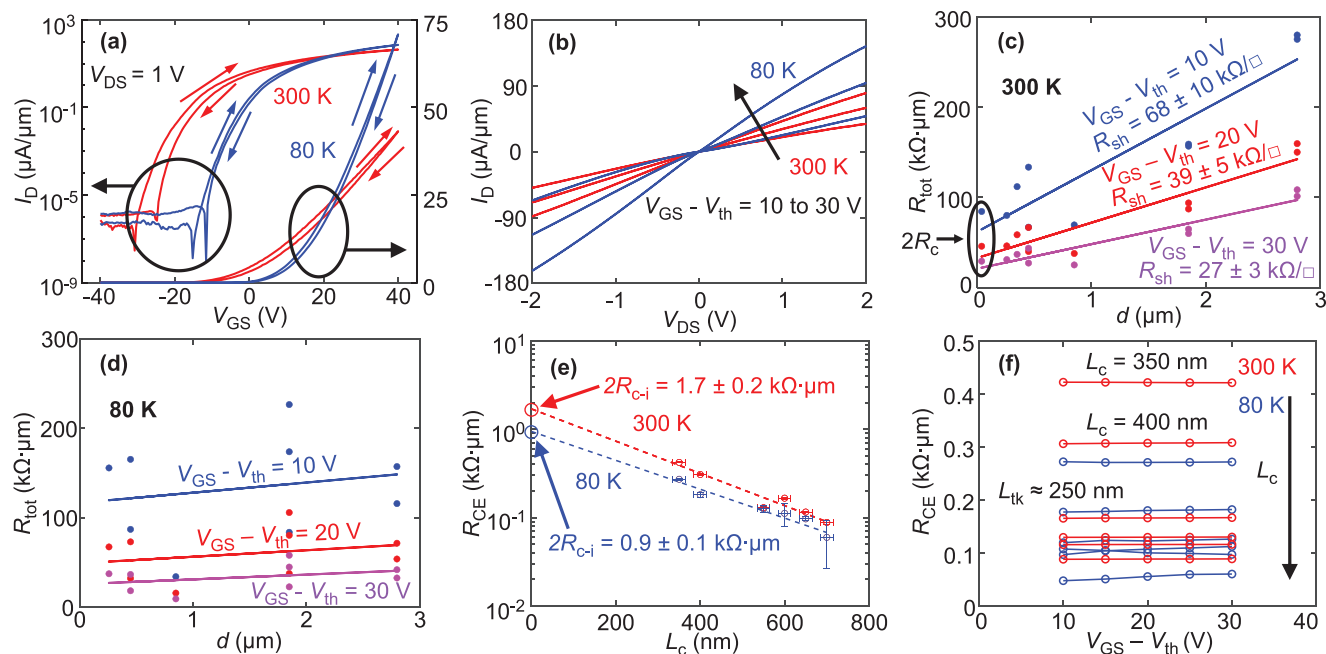


Figure 2. Electrical characteristics of MoS₂ transistors, TLM and contact-end resistance analysis. a) Linear and log-scale transfer and b) output curves of a 1 μm long MoS₂ FET at 300 K (red) and 80 K (blue). The characteristics show typical electrical behavior with minimal hysteresis. Total resistance versus channel length at c) 300 K and d) 80 K. Symbols represent measured values and the solid lines are linear fits to the data. The results include data from multiple channel arrays and therefore reflect the variation in film properties due to growth and processing damage. The contact resistance extracted at 300 K is notably lower than the one extracted at 80 K and is highly dependent on the back-gate voltage. e) Measured contact-end resistance versus contact length at 300 and 80 K. A linear behavior in log-scale is observed, dashed lines are linear regressions. f) Contact-end resistance versus overdrive voltage at 300 and 80 K. R_{ce} is independent on the back-gate voltage as was previously observed.^[30]

the threshold voltages (V_{th}) were extracted from the linear regime of the I_D-V_{GS} plot for each channel (not shown). All the following measurements were then performed for the same back-gate overdrive voltage ($V_{GS} - V_{th}$).

I_D versus V_{DS} measurements of the same channel are presented in Figure 2b, showing Ohmic characteristics at 300 K and a slight deviation at 80 K. Figure 2c,d presents the total resistance (R_{tot}) versus channel length (d) for FETs from TLM arrays at 300 and at 80 K. The TLM structure and $I-V$ curves used to extract the total channel resistances are included in Section S4 (Supporting Information). Note that due to low lithography yield these results include channel resistances from multiple TLM arrays from different parts of the sample, therefore the large spread in the measured data reflects the processing and property variations in different areas of the CVD-grown MoS_2 . Extracted from the slope and y -intercept, respectively, R_{sh} and R_c show dependency on the back-gate voltage V_{GS} , as typically observed in these structures.^[10,12] The extracted R_{sh} is lower at 80 K due to the increase in carrier mobility, also noticeable from the linear regime slopes of the I_D versus V_{GS} plots. It is noted that at 80 K the total resistance is dominated by the contact resistance R_c . The large spread seen in Figure 2d can thus be attributed to the variation in contact quality for the measured channels, hindering our ability to determine the sheet resistance from TLM.

Figure 2e shows R_{ce} versus L_c where a linear behavior in log scale is observed at both room temperature and cryogenic conditions. V_{23} versus I_{12} plots are shown in Section S5 (Supporting Information), and Figure 2f displays the extracted R_{ce} versus the gate overdrive voltage $V_{GS} - V_{th}$ for different contact lengths L_c in the same CER array. Section S6 (Supporting Information) presents R_{ce} versus L_c and R_{ce} versus gate overdrive for all contact, including the 2L MoS_2 excluded from the previously shown analysis. The trends remain the same, however the extracted values of R_{c-i} and extraction error are higher. Interestingly, R_{ce} (and consequently R_{sk} and ρ_c) is found to be independent on V_{GS} , in striking contrast to the $\approx 3\times$ decrease in

R_c and R_{sh} for the same gate bias range measured by TLM. This behavior is attributed to Fermi-level pinning by metal-induced gap states (MIGS), effectively fixing the carrier concentration in monolayer MoS_2 under the contact and hindering the charge modulation capabilities of the back-gate.^[30,37,38] Thus, the traditional TLM model (not accounting for the junction resistance) cannot explain how R_c is experimentally found to be dependent on V_{GS} . This forces us to conclude that a third component of the contact resistance, other than R_{sk} and ρ_c , must be introduced to settle this contradiction. It is this unique combination of TLM and CER measurements of contacts to atomically thin 2D semiconductor channels which uncovers the additional component of the contact resistance, which is not included in the classical transmission line model of contact resistance to bulk materials.

Our CER measurements show that the back-gate voltage modulates the energy bands with respect to the Fermi level in the MoS_2 channel, but not under the contacts. To account for the gate dependency of R_c that is shown by TLM measurements, we adopt the concept of the pseudo-junction resistance (R_{jun}) first proposed by Venica et al.^[30] and depicted in Figure 3a. R_{jun} is a series-resistance component of R_c which was originally attributed to the formation of a lateral junction between the channel and the area under the contact due to a variation in the material properties caused by the metal deposition. The variation can stem from several mechanisms such as physical damage from the deposition process, bandgap variation and Fermi level pinning by the contacting metal.^[21,22,37–39]

Here, we use R_{jun} to describe the injection resistance which includes the tunneling through, and thermionic emission over, the Schottky barrier (SB) between the metal and semiconductor. R_{jun} is a unique feature of atomically thin 2D materials, rooted in the lateral extension of the barrier directly from the contact into the channel, shown in Figure 3b.^[23,24] Figure 3c,d shows a TCAD simulation of the potential distribution near the Ni/ MoS_2 interface for 1L and 10L MoS_2 . For 1L MoS_2 the depletion is mainly lateral, which also dictates lateral current flow

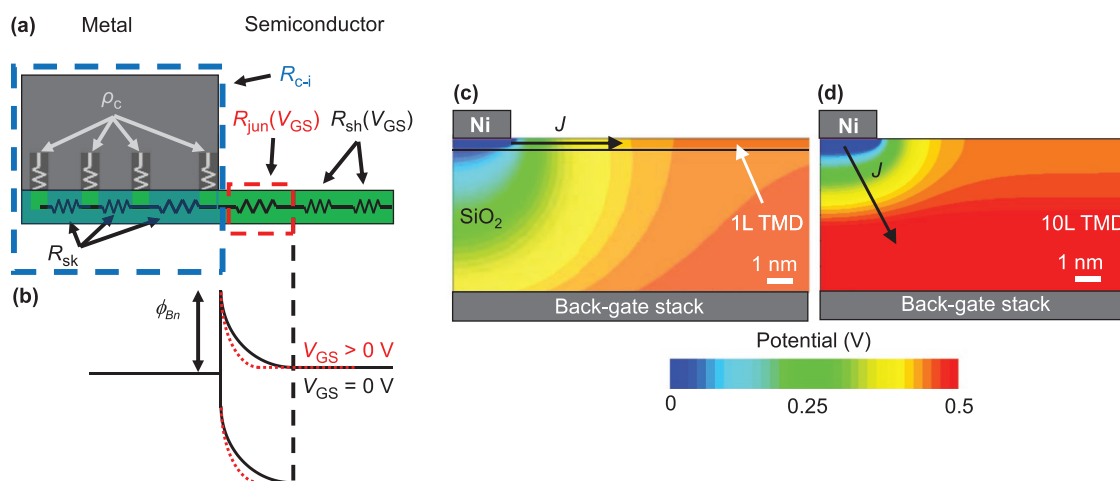


Figure 3. Cartoon and TCAD simulations illustrating the junction resistance component, R_{jun} . a) Device schematics showing where the junction resistance fits between the metal contact and the 2D semiconductor channel. The intrinsic contact resistance R_{c-i} is defined as the combined contribution of R_{sk} and ρ_c . b) Cartoon of the band diagram of the SB components of R_{jun} . The effect of the back-gate voltage is illustrated in red. The alignment of the SB for injection is depicted to emphasize the origin of R_{jun} . TCAD simulation showing the potential distribution for c) 1L and d) 10L MoS_2/Ni contact. For atomically thin MoS_2 the potential decays laterally and for thicker MoS_2 the potential also decays vertically.

from the contact, while for 10L MoS₂ the depletion (and current flow) has a significant vertical component. This reiterates that R_{jun} is most relevant for atomically thin semiconductors. Technical details about the TCAD simulation are found in Section S7 (Supporting Information) which also presents an estimation of the lateral extension of the barrier at different carrier concentrations. The barrier penetrates about 10 nm into the MoS₂ channel for a carrier concentration of $n = 5 \times 10^{10} \text{ cm}^{-2}$, however this length shortens as the back-gate voltage is increased.

Although not all components of the injection resistance are necessarily serial in nature (i.e., some components of lateral and vertical injections can be thought of being parallel to each other) we choose to lump them as R_{jun} for the sake of the simplicity of the discussion. A more complicated procedure of modeling the contribution of the junction resistance could further correct the model, but the simple series resistance assumption holds well enough for our data. We note that for cases where only lateral or vertical injection are present (e.g., pure edge contacts only exhibit lateral carrier injection) R_{jun} will be solely determined by that mechanism.

The extreme thinness of atomically thin 2D semiconductors prevents the SB from expanding vertically under the contact. We thus expect the majority of tunneling through the barrier to take place directly into the channel, even for high concentration of charge carriers under the contact that may be induced by Fermi level pinning.^[23,24] As the back-gate voltage increases, more electrons occupy the channel. Because the tunneling distance is inversely proportional to the carrier concentration, the lateral carrier injection becomes more probable and consequently the junction resistance decreases as the overdrive voltage increases, shown schematically in Figure 3b. We therefore conclude that R_{jun} is highly dependent on V_{GS} . To separate between the gate-dependent and independent components of the total contact resistance ($R_{\text{c-tot}}$, extracted from TLM) we define the intrinsic resistance under the contact ($R_{\text{c-i}}$) similar to the classical contact-front resistance R_{cf} (i.e., the contact resistance without any lateral injection)

$$R_{\text{c-i}} = R_{\text{cf}} = \frac{\sqrt{R_{\text{sk}} \rho_{\text{c}}}}{W} \quad (5)$$

as illustrated in Figure 3a, and thus $R_{\text{c-tot}}$ is comprised of $R_{\text{c-i}}$ and R_{jun} . Using this, the y -intercept of R_{ce} versus L_{c} , extrapolated from the range $L_{\text{c}} > L_{\text{tk}}$ now yields $R_{\text{ce}}(L_{\text{c}} = 0) = 2R_{\text{c-i}}$, as shown in Figure 2e. We can also extract $L_{\text{tk}} = 240 \pm 10 \text{ nm}$ at 300 K and $270 \pm 20 \text{ nm}$ at 80 K, which is quite large in the context of contact scaling, as previously discussed in depth by Schulman et al.,^[25] and will result in increased $R_{\text{c-tot}}$ which will ultimately limit the performance of ultra-scaled devices. However, this transfer length can be substantially lowered with proper engineering to reduce ρ_{c} . Furthermore, we can determine the contact resistivity and sheet resistance under the contact as $\rho_{\text{c}} = 2 \pm 0.2 \times 10^{-6} \Omega \text{ cm}^2$ at 300 K and $1.2 \pm 0.2 \times 10^{-6} \Omega \text{ cm}^2$ at 80 K, $R_{\text{sk}} = 3.5 \pm 0.5 \text{ k}\Omega \square^{-1}$ at 300 K and $1.7 \pm 0.3 \text{ k}\Omega \square^{-1}$ at 80 K. We note that this is the first time R_{sk} values are reported for 1L CVD grown MoS₂, and among the few results reported for any 2D materials.^[40–43] This R_{sk} value is low compared to the lowest reported $R_{\text{sh}}^{\text{[12]}$ due to the high carrier concentration induced by the Fermi level pinning under the contacts.

An *incorrect* extraction of R_{sk} from TLM and CER without accounting for R_{jun} is presented in Section S8 (Supporting Information). When we do not consider the lateral extension of the depletion into the channel beyond the contact “front” (R_{jun}) we get artificially large and incorrect R_{sk} values, and an unexplained R_{sk} dependency on L_{c} . This stems from the inclusion of the junction resistance effect in the TLM measurements, and therefore skewing the extraction of R_{sk} . It is of interest to note that ρ_{c} seems to be lower at 80 K, which commonly is not the case when thermionic emission dominates the carrier injection. However, considering the strong doping caused by Fermi level pinning we can see that the carrier injection is in the tunneling regime which shows a decrease in the contact resistivity at lower temperatures, as previously reported.^[44,45]

2.2. Four-Point Probe (4PP) Measurements

To extract R_{jun} we continued our characterization with 4PP measurements using the device structure shown in Figure 4a. The different contacts in this structure consist of two large-area current driving probes (1 and 4), and two small-area voltage measurement probes (2 and 3). The small size of the voltage probes and the large distance (compared to the $\approx 10 \text{ nm}$ lateral barrier extension) between them helps reducing their effect on the overall resistance (e.g., a potential drop due to the junction resistances between the voltage probes), and therefore we neglect their contribution. I - V curves measured between large (1) and small (2) terminals, presented in Figure 4b, show reduced current when charge carriers (electrons) are injected from the latter, suggesting that the current flow bottleneck is the carrier-injecting contact (source).

R_{sk} and ρ_{c} are determined only by the metal–semiconductor interface, thus their resistance contribution is expected to be independent on whether the electrode injects or collects current (acting as source or drain, respectively). In contrast, R_{jun} includes the thermionic emission over the SB that is only present where carriers are injected. Therefore, we conclude that the measured asymmetry in the I - V curves suggests that R_{jun} is more prominent at the carrier-injecting contact. We note that some asymmetry may result from contact-to-contact variation caused by fabrication and variations in the MoS₂ CVD growth, however we generally measured larger resistances at the source side by measuring the same structure with both polarities. Section S9 (Supporting Information) details a potential measurement across the 4PP device channel showing larger potential drops at the source contact compared to the drain contact, further affirming our claim.

To extract R_{jun} we applied current I_{14} between terminals (1) and (4) and probed the voltage V_{23} between terminals (2) and (3). We started by extracting the sheet resistance expressed by

$$R_{\text{sh}} = WV_{23}/I_{14}d_{23} \quad (6)$$

where d_{23} is the distance between probes (2) and (3). Then, we extracted the total contact resistance which is expressed by

$$2 R_{\text{c-tot}} = WV_{14}/I_{14} - R_{\text{sh}}d_{14} \quad (7)$$

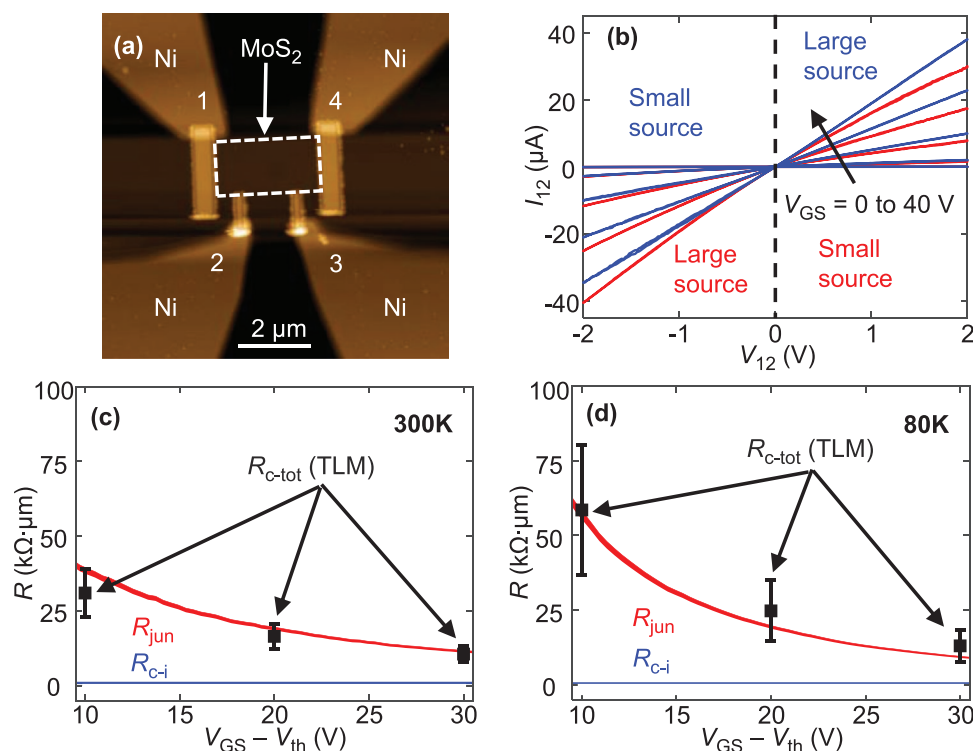


Figure 4. Four-point probe (4PP) test structure and measurement. a) AFM topography image of the 4PP measurement structure, Ni contacts, and leads are labeled. b) I - V curves between terminals (1) and (2) of the 4PP structure for $V_{GS} = 0$ to 40 V. The current is higher when the carrier injection (at the source electrode) takes place at the large terminal (1). R_{jun} and R_{c-i} versus gate overdrive voltage at c) 300 K and d) 80 K. The square symbols show R_{c-tot} obtained from TLM, and the uncertainty is represented by the error bars. The TLM values are in good agreement with R_{jun} obtained from our analysis, suggesting that R_{c-tot} is dominated by R_{jun} .

where V_{14} and d_{14} are the voltage drop and distance between contacts (1) and (4) respectively. R_{c-tot} is double-counted because the current path runs through two semiconductor-metal interfaces. Finally, R_{jun} is expressed and calculated by the following simple expression

$$R_{jun} = R_{c-tot} - R_{c-i} \quad (8)$$

where R_{c-i} is extracted from CER measurements.

R_{jun} and R_{c-i} as a function of the overdrive voltage are plotted at 300 and 80 K in Figure 4c,d, respectively. The total contact resistance values obtained from TLM are overlain for comparison (e.g., $R_{c-tot} = 31 \pm 8.1 \text{ k}\Omega \mu\text{m}$ at $V_{GS} - V_{th} = 10 \text{ V}$ and 300 K). The high contact resistance is a result of the Fermi level pinning leading to a large SB height, and R_{jun} is not reduced by any means of heavy doping or gating the access regions near the contacts. R_{jun} exhibits a strong V_{GS} dependency, expectedly decreasing as the overdrive voltage, and consequently the channel carrier density, is increased. On the other hand, R_{c-i} was found to be gate-independent during CER measurements, echoing the effect of Fermi level pinning on the carrier concentration under the contacts. It is important to note that although some electric charge is induced under the contacts by the applied back-gate voltage through a capacitive effect, it is not enough to overcome the Fermi level pinning and therefore does not affect the band diagram under the contacts. We further discuss this point later and show TCAD simulation results

to support our claim. Comparing measurements at 300 and 80 K we see that R_{jun} increases at lower temperature, in agreement with the TLM measurements, although R_{c-i} shows marginal change. This is explained by the temperature dependence of the current injection mechanism into the channel (thermionic emission and thermionic field emission^{[46])} or under the contact (tunneling^{[44,45])}. Namely, reducing the temperature decreases the thermionic emission probability and the electron effective mass, therefore increasing R_{jun} while decreasing R_{c-i} .^[44]

We can now explain that for the Ni contacts considered here, the gate-dependency of R_{c-tot} is determined by R_{jun} through the electrostatic gating of the access regions, while R_{c-i} is gate-independent owing to the Fermi level pinning. Moreover, because in our devices R_{jun} results from the large SB height between Ni and MoS₂, it is high compared to R_{c-i} and dominates R_{c-tot} , in good agreement with the TLM results. We reiterate that although our reported value of L_{tk} is 240 nm, R_{jun} is considered as a series resistance component of R_{c-tot} in atomically thin semiconductors due to the band bending extending laterally into the channel. Because the charge carriers must pass through the junction prior to traveling under the contact, R_{jun} is present in our devices and plays a role in R_{c-tot} regardless of the value of L_{tk} .

In contrast to our Ni contacts, the behavior of optimized contacts (e.g., $R_{c-tot} < 1 \text{ k}\Omega \mu\text{m}$) can be universally explained as R_{jun} is reduced and R_{c-tot} is not necessarily dominated by R_{c-i} or R_{jun} .

This is achieved by either increasing the channel carrier concentration and decreasing the SB width,^[12] or by de-pinning the Fermi level and decreasing the SB height.^[13,47] For example, Jin et al.^[48] recently explored contact gating for semi-metallic Bi contacts on WS₂, where the Fermi level is unpinned under the contacts due to the lack of MIGS at the Bi-WS₂ interface. We expect R_{c-i} to be gate dependent for such contacts. Moreover, R_{j-un} is expected to be on the same order of magnitude as R_{c-i} due to the low SB height thanks to the Bi contacts, resulting in almost no extension of the barrier into the channel.^[13] They studied a dual gated WS₂ FET which has a global back-gate that freely modulates the carrier concentration under the contacts and in the channel region, and a local top-gate that only modulates the carrier concentration in the channel region. They report that R_{c-tot} is strongly affected by the back-gate, which is readily explained by the reduction of both R_{c-i} and R_{j-un} in the case of unpinned Bi contacts. However, they also report a weaker dependency of R_{c-tot} on the top-gate voltage, which we can explain by the reduction of R_{j-un} . Their observed modulation of R_{c-tot} by the top-gate is rather weak compared to the bottom-gate because of two possible reasons. First, although R_{c-tot} is determined by both R_{c-i} and R_{j-un} due to the low SB height of the Bi contacts, the top-gate can only modulate R_{j-un} but the bottom-gate can modulate both R_{j-un} and R_{c-i} . Second, the short lateral extension of the SB into the access regions is poorly gated by the top-gate due to limitation of the device structure having top-contacts. Meaning that even if R_{c-tot} is dominated by R_{j-un} , the bottom-gate has better electrostatic control over the access regions resulting in stronger modulation of R_{c-tot} compared to the top-gate.

2.3. TCAD Simulations

Finally, we present TCAD simulations performed with Sentaurus simulation tool to further study the effect of Fermi level pinning under the contacts on R_{c-i} . Because in our Ni contacts to MoS₂ the Fermi level is pinned, the application of back-gate voltage does not change the number of electrons in that region. Therefore, it is understandable that R_{c-i} is experimentally found to be independent on V_{GS} as it is only affected by the properties of the semiconductor under the contacts. However, if the Fermi level is not fully pinned and the electrostatic doping induced by the back-gate is strong, some dependency of R_{c-i} on V_{GS} is expected. Using TCAD simulations we can estimate the number of interface traps required to pin the Fermi level. We note that the Fermi-level pinning is not forced (e.g., by specifying a strict energy location for the Fermi level), instead the Fermi level energy location is calculated by the TCAD simulator depending on the specified trap density, charge neutrality level (CNL), and boundary conditions, similar to the Bardeen model.^[49] As detailed by the model, both donor-like and acceptor-like traps are present at different energy intervals in the semiconductor bandgap at the metal interface, and the energy crossover between donor- and acceptor-like traps is defined as the CNL. If the trap concentration is high (see values below), the Fermi level will be pinned to the CNL to avoid large charge at the interface.

The device structure we used for the simulations closely resembles the work shown in previous publications.^[17,28,50]

In short, 0.6 nm thick 1L MoS₂ is defined on top of a SiO₂/Si substrate, which replicates the fabricated 1L MoS₂ devices. We model a 0.3 nm van der Waals gap between the MoS₂ layer and the metal contacts by inserting a vacuum region ($\epsilon = 1$) under the Source and Drain. The interface traps are defined by a surface concentration with a single energy level, usually placed relative to the conduction band.^[49] The simulation then solves Poisson's equation coupled with drift-diffusion equations and Fermi–Dirac statistics, and the boundary conditions we set as the applied gate and drain voltages.

Figure 5 depicts the simulated MoS₂ device band diagrams with three concentrations of interface traps ranging from $D_{it} = 10^{11}$ to $5 \times 10^{13} \text{ cm}^{-2}$. We defined both donor-like and acceptor-like traps and placed the CNL at 150 meV below the conduction band. The band diagrams show the Fermi level at the semiconductor edge under the contact as being unpinned, semi pinned, and completely pinned depending on the concentration of interface traps, similar to the Bardeen model prediction for the barrier height between metal and semiconductor.^[49] We see that for $D_{it} > 5 \times 10^{13} \text{ cm}^{-2}$ the Fermi level is pinned at the CNL and any applied V_{GS} does not change its position. Thus, the electron concentration under the contact remains constant for this concentration of interface traps. In contrast, for $D_{it} < 10^{11} \text{ cm}^{-2}$ no pinning is observed and the Fermi level is free to traverse the MoS₂ bandgap as dictated by the applied back-gate voltage. We note that the SB height in this case is still determined by the work function difference between the metal and MoS₂,^[49] and not the by back-gate. For $D_{it} = 5 \times 10^{12} \text{ cm}^{-2}$ an intermediate state is observed where the Fermi level is neither pinned nor unpinned. It is found close to the CNL, but the applied V_{GS} does affect its location. These observations are not specific to the MoS₂/Ni interface studied here, Bardeen estimated the threshold value required for pinning to be $D_{it} > 10^{13} \text{ cm}^{-2}$,^[49] and the results of our TCAD simulations coincide with the prediction. The experimental evidence of the independency of R_{c-i} on V_{GS} (i.e., Fermi level pinning) suggests that the density of interface traps at the fabricated MoS₂/Ni interfaces is larger than $\approx 5 \times 10^{13} \text{ cm}^{-2}$. Moreover, we can also project that to unpin the Fermi level, a clean interface with D_{it} of less than 10^{11} cm^{-2} is needed.

3. Conclusions

In conclusion, we have conducted TLM, CER, and 4PP measurements at room temperature and cryogenic conditions to rigorously characterize the contact resistance to monolayer MoS₂. The TLM extraction of R_{sh} and R_c showed that the contact resistance is strongly dependent on the back-gate voltage. In contrast, CER results indicated that the components of the contact resistance physically located at the metal–2D semiconductor interface, ρ_c and R_{sk} , are unaffected by gate bias which was attributed to Fermi level pinning under the contacts. We proposed that in addition to the intrinsic contact resistance components, ρ_c and R_{sk} lumped as R_{c-i} , a third component, R_{j-un} , must be introduced to explain the total contact resistance to 2D semiconductors. R_{c-i} accounts for the intrinsic metal–semiconductor interface resistance. R_{j-un} accounts for the thermionic emission over and tunneling through the

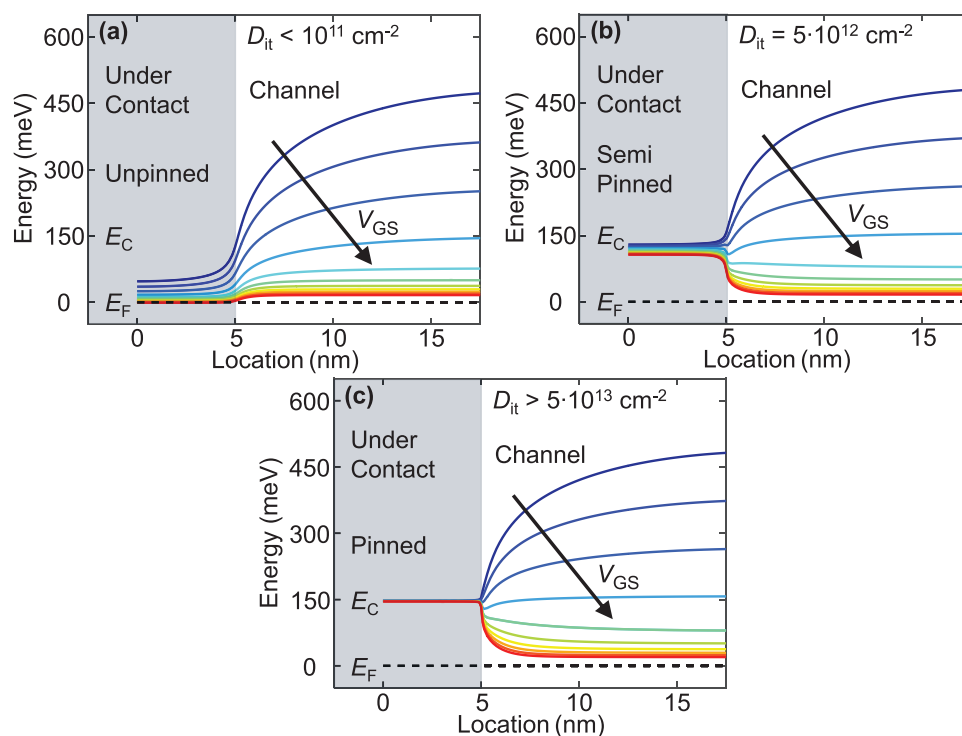


Figure 5. TCAD simulated band diagrams of MoS₂ for a) $D_{it} < 10^{11} \text{ cm}^{-2}$, b) $D_{it} = 5 \times 10^{12} \text{ cm}^{-2}$, and c) $D_{it} > 5 \times 10^{13} \text{ cm}^{-2}$. The charge neutrality level placed at 150 meV below the conduction band. The shaded area highlights the MoS₂ under the contact, and the dashed black line represents the Fermi level.

Schottky barrier at the contact edge, which in the case of atomically thin 2D semiconductor devices extends into the channel.

We performed 4PP measurements and used a simplified model to calculate and distinguish between R_{jun} and $R_{\text{c-i}}$, showing that R_{jun} expresses the gate- and temperature-dependence of the total contact resistance, while $R_{\text{c-i}}$ was found to be mostly gate-independent. Furthermore, R_{jun} dominated the contact resistance to our devices, being at least $5\times$ larger than $R_{\text{c-i}}$ for the tested gate bias range. Finally, we used TCAD simulations to study Fermi level pinning under the contacts and estimated that to achieve fully unpinned contacts, clean metal–semiconductor interfaces with $D_{it} < 10^{11} \text{ cm}^{-2}$ are desired. R_{jun} can also help explain recent reported data of state-of-the-art contact resistance reduction methods such as oxide doping,^[12] semimetallic contacts,^[13] and edge contacts.^[15] The first is explained by the increased carrier concentration near the contacts, thus lowering the tunneling distance and reducing the lateral injection resistance. The second is explained by the lowering of the Schottky barrier for injection through de-pinning of the Fermi level, again reducing the injection resistance. The last is explained by shunting the vertical charge transport and directly injecting charge carriers to the channel, essentially eliminating $R_{\text{c-i}}$. Thus, engineering contacts that take advantage of all the aforementioned methods should result in contacts with ultralow contact resistance. Therefore, by deepening the understanding of the different contact resistance components, our findings help characterize, analyze, and ultimately design better contacts to atomically thin semiconductors.

4. Experimental Section

MoS₂ Device Fabrication: MoS₂ was grown by a CVD process on SiO₂ (90 nm)/Si (p⁺⁺) substrates which also serve as global back-gate; more details on the CVD process are found in Section S10 (Supporting Information). All patterning steps were done by e-beam lithography using Raith EBPG 5200. First, 50 nm thick Ni contacts were defined and e-beam evaporated under high vacuum ($\approx 4 \times 10^{-8}$ Torr) followed by lift-off in acetone and cleaning in IPA. Second, MoS₂ was etched in RIE Plasma-Therm 790 to define the channels using 90 s O₂ plasma with 20 sccm gas flow, 10 W radio frequency (RF) power, and 20 mTorr ambient pressure. Finally, Ti/Ni/Au (15/15/20 nm) probing pads and leads were evaporated, with Ti acting as an adhesion layer. The TLM structures consist of equal length contacts ($L_c = 750 \text{ nm}$) with varying spacings ($d = 40\text{--}4800 \text{ nm}$). In the CER structure the contacts were equally spaced ($d = 350 \text{ nm}$) and vary in length ($L_c = 250\text{--}700 \text{ nm}$). The 4PP structure has two large current probes spaced $2.7 \mu\text{m}$ apart, and two voltage probes spaced $1.15 \mu\text{m}$ apart, and 330 nm from the current probes.

Characterization: The MoS₂ sample topography was first characterized using optical microscopy (Zeiss Axiotron). The Raman and second harmonic generation spectroscopy and mapping were performed with a WITec alpha300 R instrument using 532 nm laser, 1200 g mm^{-1} grating, and $100\times$ objective lens. The WITec Project FIVE software was used for analysis, and the Si peak position at 520 cm^{-1} was used for intensity normalization of all spectra. Electrical characterization was carried out with a Keysight B1500 semiconductor parameter analyzer (SPA) in a Janis probe station in vacuum conditions ($<10^{-4} \text{ mbar}$) at room temperature (near 300 K) and at cryogenic conditions (80 K).

Supporting Information

Supporting Information is available from the Wiley Online Library or from the author.

Acknowledgements

The fabrication was performed at the Technion Micro-Nano Fabrication & Printing Unit (MNF&PU) with support from the Russell Berrie Nanotechnology Institute (RBNI). The authors thank Guy Ankonina for his help with the SHG measurements. This work was supported in part by ISF grant no. 1179/20. R.W.G. acknowledges partial support from the National Science Foundation Graduate Research Fellowship Program under Grant No. DGE-1656518 and from Intel. E.P. acknowledges partial support by ASCENT, one of six centers in JUMP, an SRC program sponsored by DARPA.

Conflict of Interest

The authors declare no conflict of interest.

Author Contributions

E.B. and E.Y. conceived the experiments and wrote the manuscript with input from all authors. R.W.G. grew the MoS₂. E.B. fabricated the devices and performed electrical, PL, and Raman characterizations.

Data Availability Statement

The data that support the findings of this study are available from the corresponding author upon reasonable request.

Keywords

contact end resistance, contact resistance, four-point probe, junction resistance, transfer length method

Received: December 23, 2022

Revised: February 28, 2023

Published online: April 20, 2023

- [1] G. E. Moore, *IEEE Solid-State Circuits Soc. Newsl.* **2009**, *11*, 33.
- [2] R. H. Dennard, F. H. Gaensslen, H.-N. Yu, V. L. Rideout, E. Bassous, A. R. Leblanc, *IEEE J. Solid-State Circuits* **1974**, *9*, 256.
- [3] C. P. Auth, J. D. Plummer, *IEEE Electron Device Lett.* **1997**, *18*, 74.
- [4] A. P. Jacob, R. Xie, M. G. Sung, L. Liebmann, R. T. P. Lee, B. Taylor, *Int. J. High Speed Electron. Syst.* **2017**, *26*, 1740001.
- [5] K. Uchida, H. Watanabe, A. Kinoshita, J. Koga, T. Numata, S. Takagi, *Tech. Dig. -Int. Electron Devices Meet.*, San Francisco, CA, USA, December **2002**.
- [6] A. D. Franklin, *Science* **2015**, *349*, aab2750.
- [7] S. Salahuddin, K. Ni, S. Datta, *Nat. Electron.* **2018**, *1*, 442.
- [8] S. Das, A. Sebastian, E. Pop, C. J. Mcclellan, A. D. Franklin, T. Grasser, T. Knobloch, Y. Illarionov, A. V. Penumatcha, J. Appenzeller, Z. Chen, W. Zhu, I. Asselberghs, L.-J. Li, U. E. Avci, N. Bhat, T. D. Anthopoulos, R. Singh, *Nat. Electron.* **2021**, *4*, 786.
- [9] K. Nassiri Nazif, A. Kumar, J. Hong, N. Lee, R. Islam, C. J. Mcclellan, O. Karni, J. Van De Groep, T. F. Heinz, E. Pop, M. L. Brongersma, K. C. Saraswat, *Nano Lett.* **2021**, *21*, 3443.
- [10] C. D. English, G. Shine, V. E. Dorgan, K. C. Saraswat, E. Pop, *Nano Lett.* **2016**, *16*, 3824.
- [11] D. Somvanshi, E. Ber, C. S. Bailey, E. Pop, E. Yalon, *ACS Appl. Mater. Interfaces* **2020**, *12*, 36355.
- [12] C. J. Mcclellan, E. Yalon, K. K. H. Smithe, S. V. Suryavanshi, E. Pop, *ACS Nano* **2021**, *15*, 1587.
- [13] P.-C. Shen, C. Su, Y. Lin, A.-S. Chou, C.-C. Cheng, J.-H. Park, M.-H. Chiu, A.-Y. Lu, H.-L. Tang, M. M. Tavakoli, G. Pitner, X. Ji, Z. Cai, N. Mao, J. Wang, V. Tung, J. Li, J. Bokor, A. Zettl, C.-I. Wu, T. Palacios, L.-J. Li, J. Kong, *Nature* **2021**, *593*, 211.
- [14] A. S. Chou, P.-C. Shen, C.-C. Cheng, L.-S. Lu, W.-C. Chueh, M.-Y. Li, G. Pitner, W.-H. Chang, C.-I. Wu, J. Kong, L.-J. Li, H.-S. P. Wong, *2020 IEEE Symp. VLSI Technol.*, Honolulu, HI, USA **2020**.
- [15] A.-S. Chou, C.-C. Cheng, S.-L. Liew, P.-H. Ho, S.-Y. Wang, Y.-C. Chang, C.-K. Chang, Y.-C. Su, Z.-D. Huang, F.-Y. Fu, C.-F. Hsu, Y.-Y. Chung, W.-H. Chang, L.-J. Li, C.-I. Wu, *IEEE Electron Device Lett.* **2021**, *42*, 272.
- [16] X. Zhang, Q. Liao, Z. Kang, B. Liu, X. Liu, Y. Ou, J. Xiao, J. Du, Y. Liu, L. Gao, L. Gu, M. Hong, H. Yu, Z. Zhang, X. Duan, Y. Zhang, *Adv. Mater.* **2021**, *33*, 2007051.
- [17] A. J. Arnold, D. S. Schulman, S. Das, *ACS Nano* **2020**, *14*, 13557.
- [18] D. K. Schroder, *Semiconductor Material and Device Characterization*, Wiley, New York **2015**.
- [19] G. K. Reeves, H. B. Harrison, *IEEE Electron Device Lett.* **1982**, *3*, 111.
- [20] R. Zan, Q. M. Ramasse, R. Jalil, T. Georgiou, U. Bangert, K. S. Novoselov, *ACS Nano* **2013**, *7*, 10167.
- [21] K. Schauble, D. Zakhidov, E. Yalon, S. Deshmukh, R. W. Grady, K. A. Cooley, C. J. Mcclellan, S. Vaziri, D. Passarello, S. E. Mohney, M. F. Toney, A. K. Sood, A. Salleo, E. Pop, *ACS Nano* **2020**, *14*, 14798.
- [22] C. M. Smyth, R. Addou, S. McDonnell, C. L. Hinkle, R. M. Wallace, *J. Phys. Chem. C* **2016**, *120*, 14719.
- [23] A. Allain, J. Kang, K. Banerjee, A. Kis, *Nat. Mater.* **2015**, *14*, 1195.
- [24] A. Prakash, H. Ilatikhameneh, P. Wu, J. Appenzeller, *Sci. Rep.* **2017**, *7*, 12596.
- [25] D. S. Schulman, A. J. Arnold, S. Das, *Chem. Soc. Rev.* **2018**, *47*, 3037.
- [26] A. Rai, A. Valsaraj, H. C. P. Movva, A. Roy, R. Ghosh, S. Sonde, S. Kang, J. Chang, T. Trivedi, R. Dey, S. Guchhait, S. Larentis, L. F. Register, E. Tutuc, S. K. Banerjee, *Nano Lett.* **2015**, *15*, 4329.
- [27] C. J. L. De La Rosa, A. Nourbakhsh, M. Heyne, I. Asselberghs, C. Huyghebaert, I. Radu, M. Heyns, S. De Gendt, *Nanoscale* **2016**, *9*, 258.
- [28] G. Arutchev, C. J. L. De La Rosa, P. Matagne, S. Sutar, I. Radu, C. Huyghebaert, S. De Gendt, M. Heyns, *Nanoscale* **2017**, *9*, 10869.
- [29] G. Arutchev, P. Matagne, C. L. de la Rosa, S. Sutar, S. D. Gendt, M. Heyns, I. Radu, presented at *2017 IEEE Int. Interconnect Technology Conf.*, Hsinchu, Taiwan **2017**.
- [30] S. Venica, F. Driussi, A. Gahoi, P. Palestri, M. C. Lemme, L. Selmi, *IEEE Trans. Electron Devices* **2018**, *65*, 1589.
- [31] Á. Szabó, A. Jain, M. Parzefall, L. Novotny, M. Luisier, *Nano Lett.* **2019**, *19*, 3641.
- [32] H. H. Berger, *Solid-State Electron.* **1972**, *15*, 145.
- [33] K. K. H. Smithe, S. V. Suryavanshi, M. Muñoz Rojo, A. D. Tedjarati, E. Pop, *ACS Nano* **2017**, *11*, 8456.
- [34] Y. Li, Y. Rao, K. F. Mak, Y. You, S. Wang, C. R. Dean, T. F. Heinz, *Nano Lett.* **2013**, *13*, 3329.
- [35] W.-T. Hsu, Z.-A. Zhao, L.-J. Li, C.-H. Chen, M.-H. Chiu, P.-S. Chang, Y.-C. Chou, W.-H. Chang, *ACS Nano* **2014**, *8*, 2951.
- [36] U. Schmidt, C. S. Bailey, J. Englert, E. Yalon, G. Ankonina, E. Pop, O. Hollricher, T. Dieing, *Spectroscopy* **2021**, *36*, 23.
- [37] C. Kim, I. Moon, D. Lee, M. S. Choi, F. Ahmed, S. Nam, Y. Cho, H.-J. Shin, S. Park, W. J. Yoo, *ACS Nano* **2017**, *11*, 1588.
- [38] S. Das, H.-Y. Chen, A. V. Penumatcha, J. Appenzeller, *Nano Lett.* **2012**, *13*, 100.
- [39] A. Raja, A. Chaves, J. Yu, G. Arefe, H. M. Hill, A. F. Rigosi, T. C. Berkelbach, P. Nagler, C. Schüller, T. Korn, C. Nuckolls, J. Hone, L. E. Brus, T. F. Heinz, D. R. Reichman, A. Chernikov, *Nat. Commun.* **2017**, *8*, 15251.
- [40] S. Peng, Z. Jin, Y. Yao, L. Li, D. Zhang, J. Shi, X. Huang, J. Niu, Y. Zhang, G. Yu, *Adv. Electron. Mater.* **2019**, *5*, 1900042.

- [41] I. Moon, M. S. Choi, S. Lee, A. Nipane, J. Hone, W. J. Yoo, *2D Mater.* **2021**, *8*, 045019.
- [42] Y. Guo, Y. Han, J. Li, A. Xiang, X. Wei, S. Gao, Q. Chen, *ACS Nano* **2014**, *8*, 7771.
- [43] Y. Liu, S. Liu, Z. Wang, B. Li, K. Watanabe, T. Taniguchi, W. J. Yoo, J. Hone, *Nat. Electron.* **2022**, *5*, 579.
- [44] C. Y. Chang, Y. K. Fang, S. M. Sze, *Solid-State Electron.* **1971**, *14*, 541.
- [45] S. E. Swirhun, R. M. Swanson, *IEEE Electron Device Lett.* **1986**, *7*, 155.
- [46] C. Y. Chang, S. M. Sze, *Solid-State Electron.* **1970**, *13*, 727.
- [47] A. Kumar, K. Schauble, K. M. Neilson, A. Tang, P. Ramesh, H.-S. P. Wong, E. Pop, K. Saraswat, presented at *2021 IEEE Int. Electron Device Meeting*, San Francisco, CA, USA, December **2021**.
- [48] L. Jin, S. J. Koester, *IEEE Electron Device Lett.* **2022**, *43*, 1575.
- [49] J. Bardeen, *Phys. Rev.* **1947**, *71*, 717.
- [50] G. Mirabelli, P. K. Hurley, R. Duffy, *Semicond. Sci. Technol.* **2019**, *34*, 055015.
- [51] Z. Cheng, Y. Yu, S. Singh, K. Price, S. G. Noyce, Y. - C. Lin, L. Cao, A. D. Franklin, *Nano Lett.* **2019**, *19*, 5077.